

ASTE Observations of Warm Gas in Low-mass Protostellar Envelopes: Different Kinematics between Submillimeter and Millimeter Lines

Shigehisa TAKAKUWA*, Takeshi KAMAZAKI, Masao SAITO
*ALMA Project Office, National Astronomical Observatory of Japan,
 Osawa 2-21-1, Mitaka, Tokyo, 181-8588, Japan*

Nobuyuki YAMAGUCHI
*Nobeyama Radio Observatory, National Astronomical Observatory of Japan,
 Nobeyama, Minamimaki, Minamisaku, Nagano, 384-1305, Japan*
 and
 Kotaro KOHNO

Institute of Astronomy, The University of Tokyo, Osawa 2-21-1, Mitaka, Tokyo, 181-0015, Japan

(Received 2006 May 22; accepted 2006 July 29)

Abstract

With the ASTE telescope, we have made observations of three low-mass protostellar envelopes around L483, B335, and L723 in the submillimeter CS ($J=7-6$) and HCN ($J=4-3$) lines. We detected both the CS and HCN lines toward all the targets, and the typical CS intensity (~ 1.0 K in T_B) is twice higher than that of the HCN line. Mapping observations of L483 in these lines have shown that the submillimeter emissions in the low-mass protostellar envelope are resolved, exhibit a western extension from the central protostar, and that the deconvolved size is ~ 5500 AU \times 3700 AU (P.A. = 78°) in the HCN emission. The extent of the submillimeter emissions in L483 implies the presence of higher-temperature ($\gtrsim 40$ K) gas at 4000 AU away from the central protostar, which suggests that we need to take 2-dimensional radiative transfer models with a flattened disklike envelope and bipolar cavity into account to explain the temperature structure inside the low-mass protostellar envelope. The position-velocity diagrams of these submillimeter lines in L483 and B335 exhibit different velocity gradients from those found in the previous millimeter observations. In particular, along the axis of the associated molecular outflow the sense of the velocity gradient traced by the submillimeter lines is opposite to that of the millimeter observations or the associated molecular outflow, both in L483 and B335. We suggest that expanding gas motions at the surface of the flattened disklike envelope around the protostar, which is irradiated from the central star directly, are the origin of the observed submillimeter velocity structure.

Key words: ISM: envelopes — ISM: warm gas — ISM: kinematics — stars: formation

1. Introduction

Previous millimeter molecular-line observations have found 3000 – 10000-AU-scale molecular envelopes with both rotation and infalling gas motion around low-mass protostars (Ohashi et al. 1996 ; Ohashi et al. 1997a ; Ohashi et al. 1997b ; Takakuwa et al. 2003). These millimeter observations have probed structures and kinematics of molecular gas with a temperature of ~ 10 K and a density of $\sim 10^{4-5}$ cm $^{-3}$ in the envelopes (Takakuwa et al. 2000 ; Saito et al. 2001). However, structures and kinematics of higher-temperature ($\gtrsim 40$ K) or higher-density gas ($\gtrsim 6 \times 10^6$ cm $^{-3}$) in those envelopes, which are presumably related to the region in the vicinity of the protostar and disk system (Ceccarelli et al. 2000 ; Osorio et al. 2003), are poorly known. This is mainly because millimeter observations can not trace warm ($\gtrsim 40$ K) and

dense ($\gtrsim 6 \times 10^6$ cm $^{-3}$) regions of envelopes due to the contamination from extended low-density ($\sim 10^{4-5}$ cm $^{-3}$) and cold (~ 10 K) gas. Submillimeter observations, which can trace warm ($\gtrsim 40$ K) and dense ($\gtrsim 6 \times 10^6$ cm $^{-3}$) gas selectively, are required to investigate such regions and to study the kinematics.

For these purposes, we have made Submillimeter Array (SMA)¹ observations of low-mass protostellar envelopes around L1551 IRS5 and IRAS 16293-2422 in the CS ($J = 7-6$; 342.9 GHz) and HCN ($J = 4-3$; 354.5 GHz) lines, respectively (Takakuwa et al. 2004 ; Takakuwa et al. 2006). These submillimeter molecular lines trace gas temperatures above $\gtrsim 40$ (K) and densities above $\gtrsim 6 \times 10^6$ cm $^{-3}$, and hence are appropriate tracers for our study. Both in L1551 IRS5 and IRAS 16293-2422, we have de-

¹ The Submillimeter Array (SMA) is a joint project between the Smithsonian Astrophysical Observatory and the Academia Sinica Institute of Astronomy and Astrophysics, and is funded by the Smithsonian Institution and the Academia Sinica.

* e-mail: s.takakuwa@nao.ac.jp

tected a compact (~ 500 AU) disklike structure associated with the protostars in the submillimeter lines. However, our SMA data recover only $\sim 11\%$ and $\sim 30\%$ of the total flux observed with JCMT in L1551 IRS5 and IRAS 16293-2422, respectively, which implies that there is also an extended (> 2000 AU) submillimeter component in the low-mass protostellar envelopes. In fact, our JCMT mapping observations of IRAS 16293-2422 in the HCN (4-3) emission have revealed an extended (~ 3000 AU) envelope structure as well as the compact (~ 500 AU) disklike structure which is embedded in the extended envelope. These results suggest that there is extended (> 2000 AU) warm ($\gtrsim 40$ K) or dense ($\gtrsim 6 \times 10^6$ cm $^{-3}$) gas as well as the compact disklike structure in these low-mass protostellar envelopes. It seems to be difficult to make gas temperatures high enough strictly via heating from the central stars embedded in the envelopes (e.g., Lay et al. 1994), and it is a puzzle why such warm ($\gtrsim 40$ K) or dense ($\gtrsim 6 \times 10^6$ cm $^{-3}$) gas can be so extended in the low-mass protostellar envelopes. These results suggest that we need to re-consider the origin of submillimeter emissions in low-mass protostellar envelopes.

In order to clarify the extent, kinematics, and the origin of submillimeter emissions in low-mass protostellar envelopes unambiguously, we have initiated mapping observations of low-mass protostellar envelopes in the HCN (4-3) and CS (7-6) lines with ASTE (Atacama Submillimeter Telescope Experiment), a new and powerful submillimeter single-dish telescope at the Atacama Site in Chile. In this paper, we report ASTE results of HCN (4-3) and CS (7-6) observations of three nearby (≤ 300 pc) low-mass protostellar sources, that is, L483, B335, and L723. L483 is a bright ($L_{bol} \sim 14 L_\odot$) Class 0 object with an East (red) - West (blue) molecular outflow at a distance of 200 pc (Ladd et al. 1991; Hatchell et al. 1999; Tafalla et al. 2000). Millimeter CS (2-1) and H₂CO (2₁₂-1₁₁, 3₁₂-2₁₁) spectra toward the protostar of L483 exhibit the "infalling asymmetry" with the stronger blueshifted emission and the absorption dip, and this source is considered to be one of the protostellar candidates with an infalling gas motion in the surrounding envelope (Myers et al. 1995; Mardones et al. 1997). Mapping observations of L483 in centimeter and millimeter lines such as NH₃ (1,1; 2,2), N₂H⁺ (1-0) and CH₃OH (2-1) have revealed that the protostellar envelope is extended along the east-west direction, and that the velocity structure is similar to that of the associated molecular outflow, suggesting that the dense gas in the outer portion of the envelope is being swept-up by the associated outflow (GregerSEN et al. 1997; Fuller & Wootten 2000; Park et al. 2000; Tafalla et al. 2000). In L483, detailed studies of chemical differentiation in the envelope have also been performed (Jørgensen et al. 2002; Jørgensen 2004). B335 is a close ($d \sim 250$ pc) Bok globule associated with a far-infrared source (IRAS 19347+0727; $L_{bol} \sim 3 L_\odot$), and its spectral energy distribution classifies this source as a Class 0 object (Davidson 1987; Barsony 1995). This source has an East (blue) - West (red) molecular outflow (Hirano et al. 1992; Chandler & Sargent 1993). Aperture synthe-

sis observations of the millimeter H¹³CO⁺ emission (Saito et al. 1999), as well as the shape of the central spectra in the CS (2-1, 3-2, 5-4) lines (Choi et al. 1995; Zhou 1995; Evans et al. 2005), have shown that there is an infalling gas motion in the surrounding envelope around B335, although the CS results may be severely affected by the contamination from the molecular outflow (Wilner et al. 2000). Detailed millimeter continuum studies in the context of the circumstellar disk and envelope have also been performed in B335 (Harvey et al. 2003a; Harvey et al. 2003b). L723 is another Class 0 candidate with a luminosity of $\sim 3L_\odot$ at a distance of 300 pc (Davidson 1987). In L723, there are two radio sources, VLA1 and VLA2 (Anglada et al. 1991), where only VLA2 is associated with the surrounding molecular envelope as well as the quadrupolar CO outflow, suggesting that VLA2 is younger than VLA1 (Hayashi et al. 1991; Hirano et al. 1998).

We note that only limited single-dish mapping observations of low-mass protostellar envelopes in submillimeter molecular lines have been reported (Hogerheijde et al. 1998; Hogerheijde et al. 1999), and that most submillimeter single-dish studies of low-mass protostellar envelopes are single-point observations, on the assumption that submillimeter lines in low-mass protostellar envelopes are more compact than the beam size of the single-dish telescopes ($< 20'' \sim 4000$ AU in nearby sources) (Blake et al. 1994; Moriarty-Schieven et al. 1995; van Dishoeck et al. 1995). Our new high-sensitivity mapping observations of the low-mass protostellar envelopes in the submillimeter lines with ASTE provide us a new insight of the origin of the submillimeter emission in low-mass protostellar envelopes, as will be shown in the present paper.

2. Observations

With the ASTE 10-m telescope we made HCN ($J = 4-3$; 354.505480 GHz) and CS ($J = 7-6$; 342.882866 GHz) observations of L483, B335, and L723 on August 16-20, 2005. Details of the ASTE telescope are presented by Ezawa et al. (2004). Table 1 summarizes the observational parameters. A cartridge-type 350 GHz receiver mounted on ASTE is a double sideband instrument with an IF frequency range of 5 to 7 GHz (Kohno 2005), and the HCN and CS lines were observed simultaneously at different sidebands. In L483 and B335, we made mapping observations centered on the protostellar positions at a grid spacing of 10'', providing Nyquist-sampled maps. The total number of observed points are 34 and 21 in L483 and B335, respectively, which covers most of the line-emitting regions. In L723 we only made a single-point observation toward the protostellar position. The telescope pointing was checked at every ~ 2 hours by making continuum observations of Jupiter and Uranus, and was found to be better than 2'' during the whole observing period. As a standard source we also observed IRAS 16293-2422 after each pointing run, and confirmed that the relative intensity is consistent within $\sim 40\%$. We compared the observed HCN and CS spectra toward IRAS 16293-2422

Table 1. Parameters of the ASTE Observations

Parameter	Value			
Observing Date	August 16-20, 2005			
Target	L483	B335	L723	IRAS 16293-2422 (Calibrator)
Right Ascension (J2000)	18 ^h 17 ^m 29 ^s .86	19 ^h 37 ^m 00 ^s .94	19 ^h 17 ^m 53 ^s .62	16 ^h 32 ^m 22 ^s .87
Declination (J2000)	-04°39'38".7	07°34'08".8	19°12'19".5	-24°28'36".6
Distance to the Target	200 pc	250 pc	300 pc	160 pc
Molecular Line	HCN ($J=4-3$; 354.50548 GHz) & CS ($J=7-6$; 342.882866 GHz)			
Spatial Resolution	$\sim 22''$			
Spectral Resolution	125 kHz ($\sim 0.11 \text{ km s}^{-1}$)			
Main Beam Efficiency	$\sim 60\%$			
Integration Time (center)	15.0 min	15.5 min	23.7 min	~ 3 min at each run
Integration Time (mapping)	~ 10 min	~ 7.5 min	-	-
rms (mapping)	$\sim 0.13 \text{ K}$ in T_B	-	-	figure1.eps
Typical System Temperature (DSB)	200 - 500 K			
Pointing Error	$< 2''$			
Pointing Source	Jupiter, Uranus			

to those obtained with the CSO telescope which has the same dish size as that of the ASTE telescope (Blake et al. 1994 ; van Dishoeck et al. 1995), and found that the main beam efficiency of the ASTE telescope was ~ 0.6 . We also confirmed that the asymmetric spectral shapes in IRAS 16293-2422 taken with the ASTE telescope are in excellent agreement with those taken with the CSO telescope. Hereafter we show observed line intensities in the unit of T_B .

3. Results

3.1. HCN and CS Spectra

In Figure 1, we show HCN (4-3) and CS (7-6) spectra toward the protostellar positions of L483, B335, and L723. We succeeded to detect these submillimeter lines in all the three low-mass protostars. In Table 2, we summarize line parameters of these submillimeter spectra derived from the Gaussian fittings. At the central protostellar positions, intensities of the CS line range from 0.8 to 1.8 K while intensities of the HCN line are more than a factor of two weaker (0.3 - 0.8 K). The CS-to-HCN intensity ratio is roughly constant (2.1 - 2.5) across the three samples, and there may be a slight correlation between the source luminosity and the line intensities. On the other hand, line widths of the HCN line are almost twice wider than the CS line widths in L483 and L723, but much narrower in B335. The HCN (4-3) line consists of six hyperfine components, two of which ($F = 3-3$ and $4-4$) can be separated from the main line ($F = 4-3$) in our data by 1.977 MHz (-1.67 km s^{-1}) and -1.610 MHz (1.36 km s^{-1}), respectively (Jewitt et al. 1997). The intensity ratio between the main and the other two hyperfine lines at the local thermal equilibrium condition is 0.0217 (Jewitt et al. 1997), and these weaker hyperfine lines are unlikely to be detectable with the present observations. However, it is still possible that the broader HCN line widths found in L483 and L723 are due to the presence of the hyperfine

Fig. 1. HCN (4-3) (upper) and CS (7-6) (lower) spectra toward the protostellar positions of L483 (left), B335 (middle), and L723 (right), taken with ASTE.

lines, if there is any hyperfine anomaly and the intensities of the $F = 3-3$ and $4-4$ lines are significantly larger than the statistical values in L483 and L723. As will be shown in the next section, the velocity structure traced by the HCN line is consistent with that traced by the CS (7-6) line without any hyperfine component, so the presence of the hyperfine components in the HCN line is unlikely to have significant impact on the investigation of the velocity structures. Systemic velocities derived from the HCN line are also consistent with those derived from the CS line, as well as those from millimeter lines of N_2H^+ (1-0) (Mardones et al. 1997) and H^{13}CO^+ (3-2) (Gregersen et al. 1997).

3.2. Spatial and Velocity Structures of the Submillimeter HCN and CS Emission

3.2.1. L483

In Figure 2, we show total integrated intensity maps of the HCN (4-3) and CS (7-6) emission in L483, along with the line profile maps of the HCN (4-3) and CS (7-6) emission in Figure 3 and 4, respectively. There appears a western extension both in the HCN and CS emissions, which is consistent with the emission distribution in the 450 μm

Table 2. Gaussian-Fitted Line Parameters of the Observed Submillimeter Emission

Source	HCN ($J=4-3$)			CS ($J=7-6$)		
	T_B (K)	V_{LSR} (km s $^{-1}$)	Δv (km s $^{-1}$)	T_B (K)	V_{LSR} (km s $^{-1}$)	Δv (km s $^{-1}$)
L483 Center	0.84	5.62	2.09	1.80	5.52	1.36
L483 -20''*	0.51	5.59	1.40	0.40	5.94	1.07
L483 average [†]	0.57	5.64	1.90	0.82	5.59	1.24
B335 Center	0.58	8.06	0.69	1.20	8.18	1.49
L723 Center	0.31	11.02	3.05	0.79	11.25	1.52

* Position at the 20'' west of the protostar.

† Averaged over the central 20'' \times 30'' region, where the central protostar locates at 10'' west and 10'' north from the bottom-left corner of the region.

continuum map (Jørgensen 2004). The intensity distribution both in the HCN and CS emission is clearly different from that of the circular beam shown at the bottom right corner of each panel in Figure 2, which suggests that the structures traced by these submillimeter lines are resolved with the present observations in L483. The deconvolved size of the HCN emission measured from a 2-dimensional Gaussian fitting to the image is 5500 \times 3700 (AU) (P.A. = 78°), while in the CS emission only the major axis is resolved (\sim 2300 AU).

In Figure 5, we show Position-Velocity (P-V) diagrams passing through the central stellar position perpendicular and parallel to the axis of the associated molecular outflow (E-W; see Figure 2) (Buckle et al. 1999 ; Hatchell et al. 1999 ; Tafalla et al. 2000). There appears velocity gradients in the CS and HCN emission both across and along the direction of the associated outflow. Perpendicular to the outflow, the northern part is blueshifted while the southern part is redshifted, and along the outflow axis the eastern part appears blueshifted and the western part redshifted. Although the loci of the velocity gradients shown in Figure 5 are somewhat arbitrary, these trends are also evident in the line profile maps of Figure 3 and 4. Across the outflow axis, similar velocity gradients are also seen in the 3-mm counterpart of the CS (2-1) line (Jørgensen 2004) and in the 3-mm C₃H₂ (2₁₂-1₀₁) line (Park et al. 2000). The amount of the velocity gradient observed in the submillimeter CS and HCN lines is measured to be \sim 230 km s $^{-1}$ pc $^{-1}$, which is much larger than that in the 3-mm C₃H₂ line (\sim 10 km s $^{-1}$ pc $^{-1}$) even though the spatial resolution of their 3-mm observations (= 14'' \times 10'') is slightly better than ours (Park et al. 2000). At higher spatial resolution (\sim 7''), the velocity gradient in the 3-mm counterpart of the CS (2-1) line is measured to be \sim 410 km s $^{-1}$ pc $^{-1}$ (Jørgensen 2004), twice higher than that obtained by our lower-resolution submillimeter observations. These velocity gradients most likely trace rotational gas motion around the protostar at different radii.

Along the outflow axis, the velocity gradient is measured to be \sim 10 km s $^{-1}$ pc $^{-1}$ in these submillimeter lines.

figure2.eps

Fig. 2. Total integrated intensity maps (integrated velocity range 4.2 - 6.9 km s $^{-1}$) of the HCN (4-3) (left) and CS (7-6) (right) emission in L483. Contour levels are 2, 4, 6 σ , and then 10 σ in steps of 4 σ (1 σ = 0.0733 K km s $^{-1}$). The highest contour in the HCN map is 18 σ and that in the CS map 34 σ . Crosses indicate observed positions, and open circles at the bottom right corner beam sizes. Red and blue arrows show the direction of the redshifted and blueshifted molecular outflow, respectively, and the roots of the arrows indicate the protostellar position.

Interestingly, in the 3-mm counterpart of the CS (2-1) line and other 3-mm lines such as N₂H $^{+}$ (1-0) the eastern part shows redshifted emission and vice versa, and the velocity gradient is measured to be \sim 280 km s $^{-1}$ pc $^{-1}$ (Jørgensen 2004). Hence, the velocity gradient traced by the submillimeter lines is opposite to that traced by the millimeter lines. The associated molecular outflow observed in CO (2-1; 4-3) lines shows redshifted emission at the east of the protostar and blueshifted emission as well as the K' reflection nebula at the west (Hatchell et al. 1999 ; Tafalla et al. 2000). Therefore, the velocity gradient in the submillimeter lines is also opposite to that of the associated outflow. In L483, the E-W velocity gradient traced by millimeter lines and CO lines is interpreted as a motion of the outflowing gas and the entrained dense gas (Fuller & Wootten 2000 ; Tafalla et al. 2000 ; Jørgensen 2004). The different velocity gradient found in our submillime-

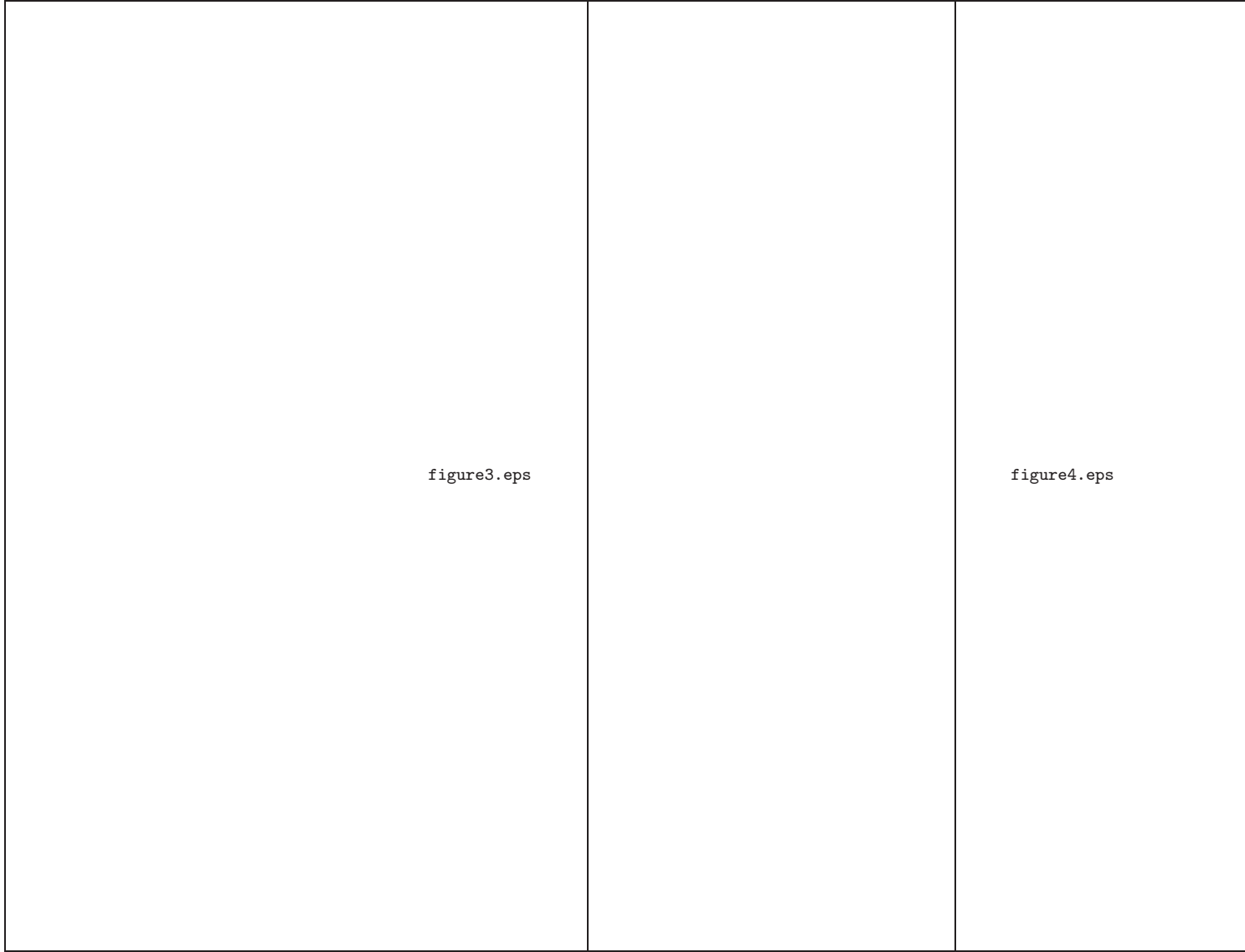


Fig. 3. Line profile map of the HCN (4–3) emission in L483. Positions of each spectrum are shown as crosses in Figure 2. Solid horizontal lines show zero levels, and dashed vertical lines systemic velocity of 5.6 km s^{-1} . 3-channel bindings are performed to increase the signal-to-noise ratio of the spectra.

Fig. 4. Same as Figure 3 but for the CS (7–6) emission.

ter observations suggest that the submillimeter emissions trace a different gas component.

3.2.2. B335

Figure 6, Figure 7 and 8 show total integrated intensity maps and line profiles maps of the HCN (4–3) and CS (7–6) emission in B335. In B335, we could not spatially resolve the structure traced by these submillimeter lines. The CS line intensity, as well as the CS line width, is much larger than those of the HCN line. Figure 9 shows P-V diagrams passing through the central stellar position across and along the axis of the the associated molecular outflow in B335 (E-W; see Figure 6) (Hirano et al. 1992 ; Chandler & Sargent 1993). In the CS emission, there appears velocity gradients both across and along the direction of the associated outflow, whereas the HCN emission is too weak to trace the velocity structure. Perpendicular to the outflow, the northern part is blueshifted while the southern

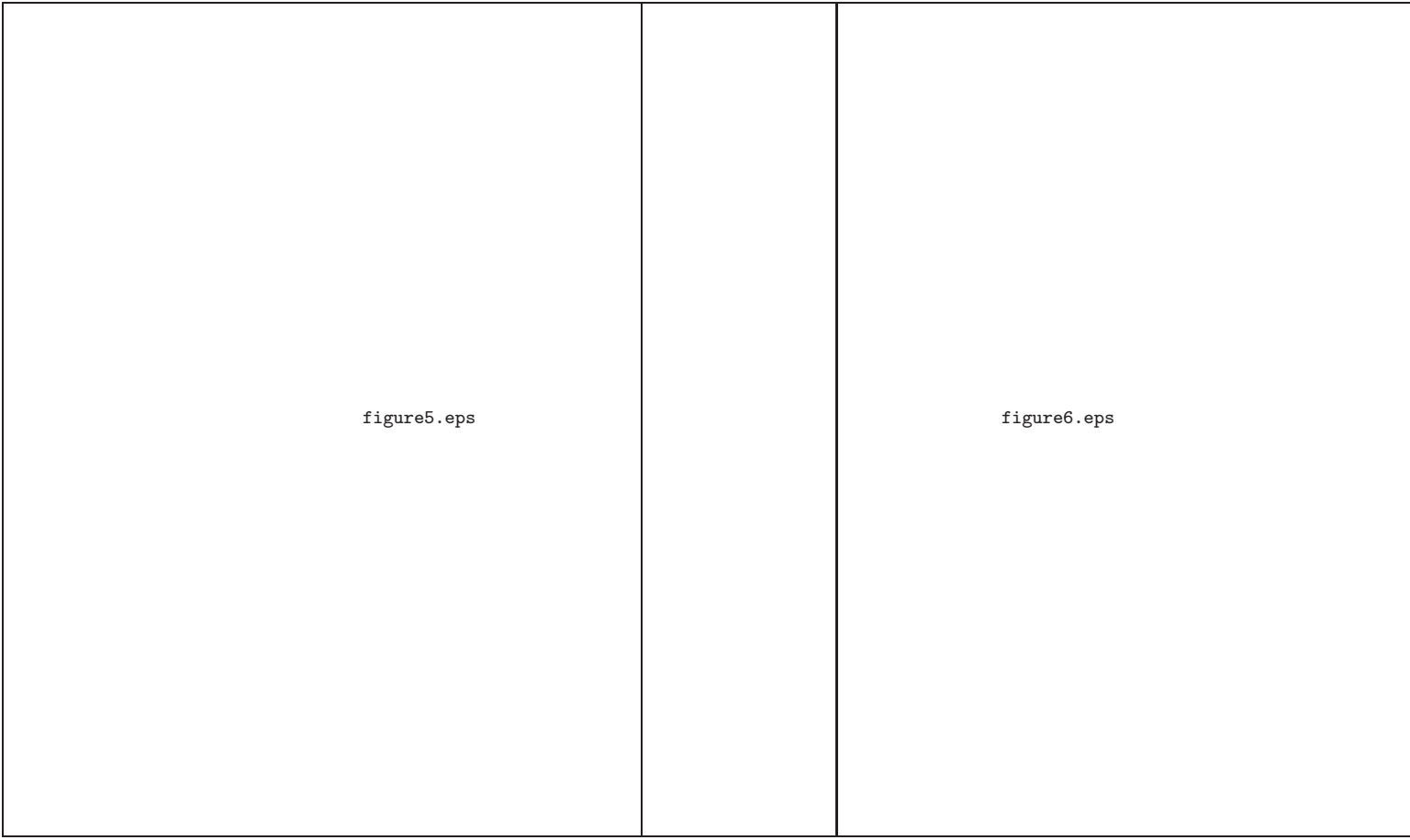


Fig. 5. Position-velocity (P-V) diagrams of the CS (left) and HCN (right) line across (upper) and along (lower) the axis of the associated molecular outflow passing through the central stellar position in L483. Contour levels are from 2σ in steps of 2σ ($1\sigma = 0.133$ K). Dashed lines delineate detected velocity gradients.

part is redshifted, and along the outflow axis the western part appears to be blueshifted and the eastern part redshifted. These velocity gradients are also seen in the line profile map of Figure 8.

Across the outflow axis, the velocity gradient traced by the submillimeter CS line (~ 160 km s $^{-1}$ pc $^{-1}$) has an opposite sense to that traced by the millimeter H 13 CO $^+$ (1-0) line, that is, in the H 13 CO $^+$ line the northern part is redshifted and the southern part blueshifted (~ 50 km s $^{-1}$ pc $^{-1}$) (Saito et al. 1999). The same trend is also seen along the outflow axis. In the submillimeter CS emission the western part is blueshifted and the eastern part redshifted (~ 110 km s $^{-1}$ pc $^{-1}$), while in the millimeter H 13 CO $^+$ emission the western part is redshifted and vice versa (~ 780 km s $^{-1}$ pc $^{-1}$) (Saito et al. 1999). Aperture synthesis images in the optically thick 13 CO (1-0) line show well-separated blue- and redshifted outflow lobes at the east and west of the protostar of B335, respectively (Chandler & Sargent 1993). Hence the velocity gradient revealed by our submillimeter observations is also opposite

Fig. 6. Total integrated intensity maps (integrated velocity range 6.8 - 9.4 km s $^{-1}$ in the CS emission and 7.7 - 8.3 km s $^{-1}$ in the HCN emission) of the HCN (4-3) (left) and CS (7-6) (right) emission in B335. Contour levels are 2, 4, 6, 10σ , and then 10σ in steps of 4σ ($1\sigma = 0.0733$ K km s $^{-1}$). The highest contour in the CS map is 22σ . Crosses indicate observed positions, and open circles at the bottom right corner beam sizes. Red and blue arrows show the direction of the redshifted and blueshifted molecular outflow, respectively, and the roots of the arrows indicate the protostellar position.

to that of the associated outflow. The E-W velocity gradient traced by the millimeter H 13 CO $^+$ line is interpreted as an infalling gas motion in the flattened disklike envelope surrounding the protostar, perpendicularly to the axis of the associated molecular outflow (Saito et al. 1999). The different velocity gradient in the submillimeter CS line implies the different origin of the gas motion from the infalling gas.

These ASTE results in L483 and B335 may suggest that the millimeter and submillimeter lines trace different gas components with different kinematics in the low-mass protostellar envelopes. On the other hand, we need further observational confirmation to verify the presence of the different velocity structure, since the spatial resolution as well as the calibration accuracy of the present submillimeter observations are limited. High-resolution imaging observations with ALMA are crucial to unambiguously

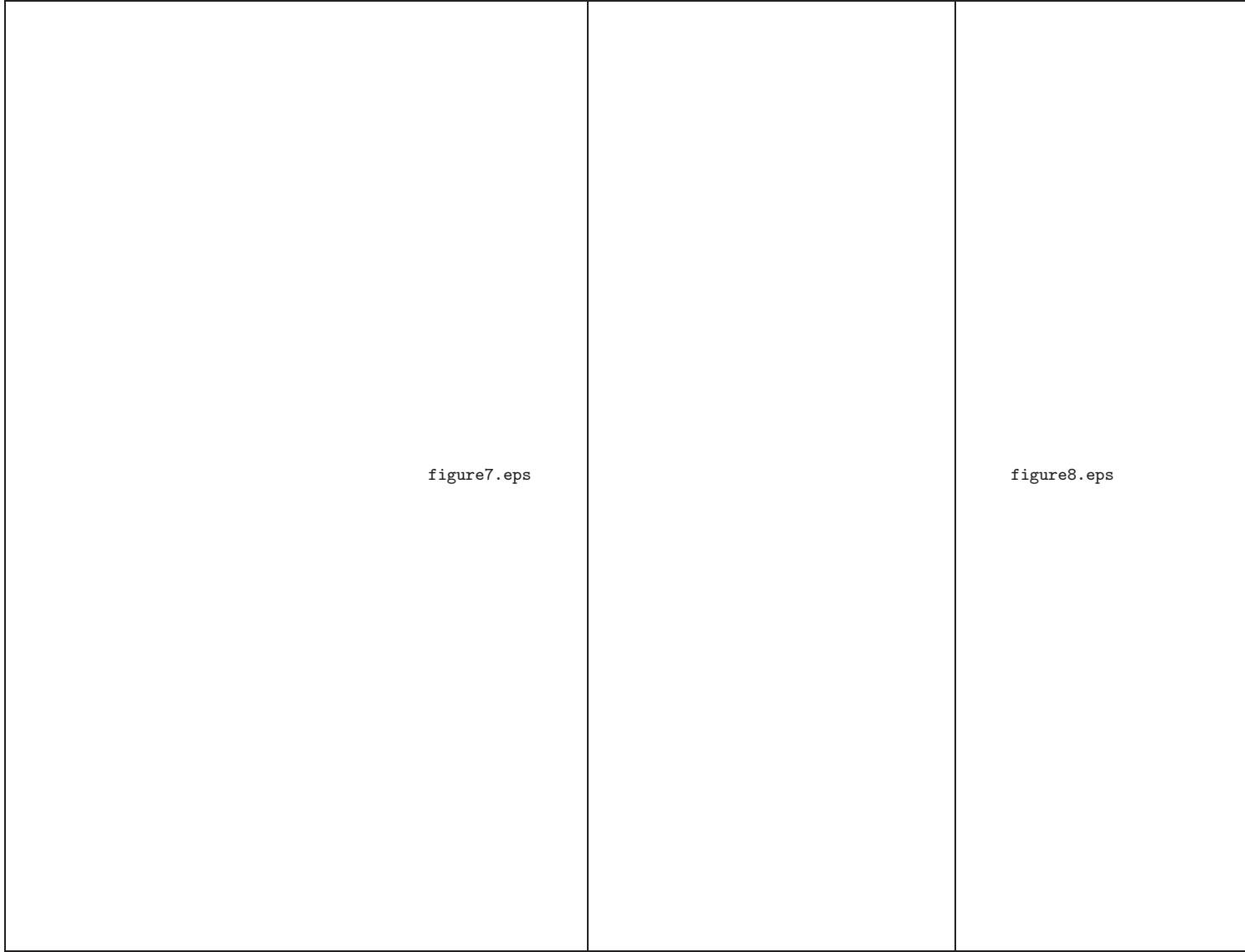


Fig. 7. Line profile map of the HCN (4–3) emission in B335. Positions of each spectrum are shown as crosses in Figure 6. Solid horizontal lines show zero levels, and dashed vertical lines systemic velocity of 8.1 km s^{-1} . 3-channel bindings are performed to increase the signal-to-noise ratio of the spectra.

Fig. 8. Same as Figure 7 but for the CS (7–6) emission.

clarify the velocity structure and the origin of the submillimeter emissions in the low-mass protostellar envelopes.

4. Discussion

4.1. *Physical Conditions of Molecular Gas traced by the Submillimeter Lines in the Low-mass Protostellar Envelopes*

Our ASTE observations have resolved the spatial and/or kinematical structures of the submillimeter HCN and CS emission in L483 and B335. The intensities and extents should trace structures of gas densities, temperatures, and molecular abundances in these envelopes. In order to investigate these physical conditions of the protostellar envelopes traced by the extended submillimeter emissions, we performed statistical equilibrium calculations of the submillimeter lines based on the Large

$X_{CS} = 6.8 \times 10^{-10}$, respectively (Jørgensen et al. 2004). The observed HCN and CS line width ($\equiv dv$) at the center of L483 is $\sim 2.1 \text{ km s}^{-1}$ and 1.4 km s^{-1} (§3.1) and the deconvolved size ($\equiv dr$) along the major axis of the HCN and CS emission is 0.027 pc and 0.011 pc (§3.2). Hence, the $X/dv/dr$ value can be derived to be $\sim 2.6 \times 10^{-11}$ for HCN and $\sim 5.6 \times 10^{-12}$ for CS. Then, at the $20'' = 4000 \text{ AU}$ west from the central protostar of L483 where the HCN and CS lines are detected to be 0.51 (K) and 0.40 (K) , respectively (Table 2), the value of n_{H2} must be higher than $\sim 6 \times 10^6 \text{ cm}^{-3}$ if $T_k = 10 \text{ (K)}$, or the value of T_k must be higher than $\sim 40 \text{ (K)}$ if $n_{H2} = 6 \times 10^5 \text{ cm}^{-3}$. At the central protostellar positions of L483 and B335, the same $X/dv/dr$ values provide the estimate of $n_{H2} > 10^7 \text{ cm}^{-3}$ if $T_k \sim 10 \text{ (K)}$, or the estimate of $T_k > 40 \text{ (K)}$ if $n_{H2} \sim 10^6 \text{ cm}^{-3}$, averaged over the $22''$ ASTE beam. These arguments imply that high-density ($\gtrsim 6 \times 10^6 \text{ cm}^{-3}$) or high-temperature ($\gtrsim 40 \text{ K}$) molecular gas could be more extended than $\sim 2000 \text{ AU}$ in radius, particularly evident at the 4000 AU west from the protostar of L483.

The presence of such an extended high-density or high-temperature gas in low-mass protostellar envelopes is also supported by other recent submillimeter-line observations of low-mass protostellar envelopes. Takakuwa et al. (2006) have made single-dish and interferometric observations of IRAS 16293-2422 in the HCN (4-3) line with the JCMT and the SMA and have found that there is an extended ($> 3000 \text{ AU}$) HCN emission plus compact ($\sim 500 \text{ AU}$) disklike structure associated with the protostar. CS (7-6) observations of L1551 IRS5 with the SMA imply that the submillimeter CS emission is more extended than $\sim 1500 \text{ AU}$ (Takakuwa et al. 2004). However, it is still less clear why these submillimeter molecular lines which trace high-density or high-temperature gas can be so extended. Masunaga et al. (1998, 2000) have constructed a one-dimensional radiation hydrodynamic model in the formation of an 1 M_\odot protostar. Their model suggests that during the main accretion phase the T_k and n_{H2} values at the radius of 4000 AU (i.e., L483 $20''$ west) are $\sim 15 \text{ K}$ and $\sim 2 \times 10^5 \text{ cm}^{-3}$, and at the radius of 2000 AU $\sim 20 \text{ (K)}$ and $\sim 10^6 \text{ cm}^{-3}$, respectively. These theoretically-predicted values seem to be slightly lower to explain the observed submillimeter emissions, although the limited spatial resolution as well as the only single transitions of our ASTE data prevents us from making direct comparison between the observational and theoretical results. On the other hand, the western extension of the submillimeter emission in L483 seems to be aligned with the western component of the associated outflow (Tafalla et al. 2000; Jørgensen 2004), and there might be another heating mechanism such as shocks due to the interaction between the outflow and the ambient gas (Umemoto et al. 1992; Hirano & Taniguchi 2001).

As described in §3.2 the velocity structures traced by the submillimeter lines are different from those traced by millimeter lines both in L483 and B335, which suggests that the submillimeter emissions have a different origin and that the spherically-symmetric radiation hy-

figure9.eps

Fig. 9. P-V diagrams of the CS (left) and HCN (right) line across (upper) and along (lower) the axis of the associated molecular outflow passing through the central stellar position in B335. Contour levels are from 2σ in steps of 2σ ($1 \sigma = 0.133 \text{ K}$). Dashed lines delineate detected velocity gradients.

Velocity Gradient (LVG) model (Goldreich & Kwan 1974; Scoville & Solomon 1974).

For the model calculations, we employed values of the dipole moment, rotational and centrifugal constants of the HCN and CS molecule listed by Winnewisser et al. (1979). Collisional transition rates of HCN were taken from Green and Thaddeus (1974) and those of CS from Green and Chapman (1978). Rotational energy levels included in our calculations are up to $J = 8$ (153 K) for HCN and $J = 13$ (214 K) for CS. These energy levels are high enough to discuss physical conditions of molecular gas in low-mass protostellar envelopes (Moriarty-Schieven et al. 1995).

In Figure 10, we show results of our calculations. The HCN and CS line intensities increase monotonically as the gas density ($\equiv n_{H2}$), molecular abundance per unit velocity gradient ($\equiv X/dv/dr$), or the gas kinetic temperature ($\equiv T_k$) increases. Since we have only one transition of HCN and CS, we cannot fully constrain the physical conditions traced by these submillimeter lines, but we can still make some arguments as follows. In L483, the HCN and CS abundance is estimated to be $X_{HCN} = 2.0 \times 10^{-9}$ and

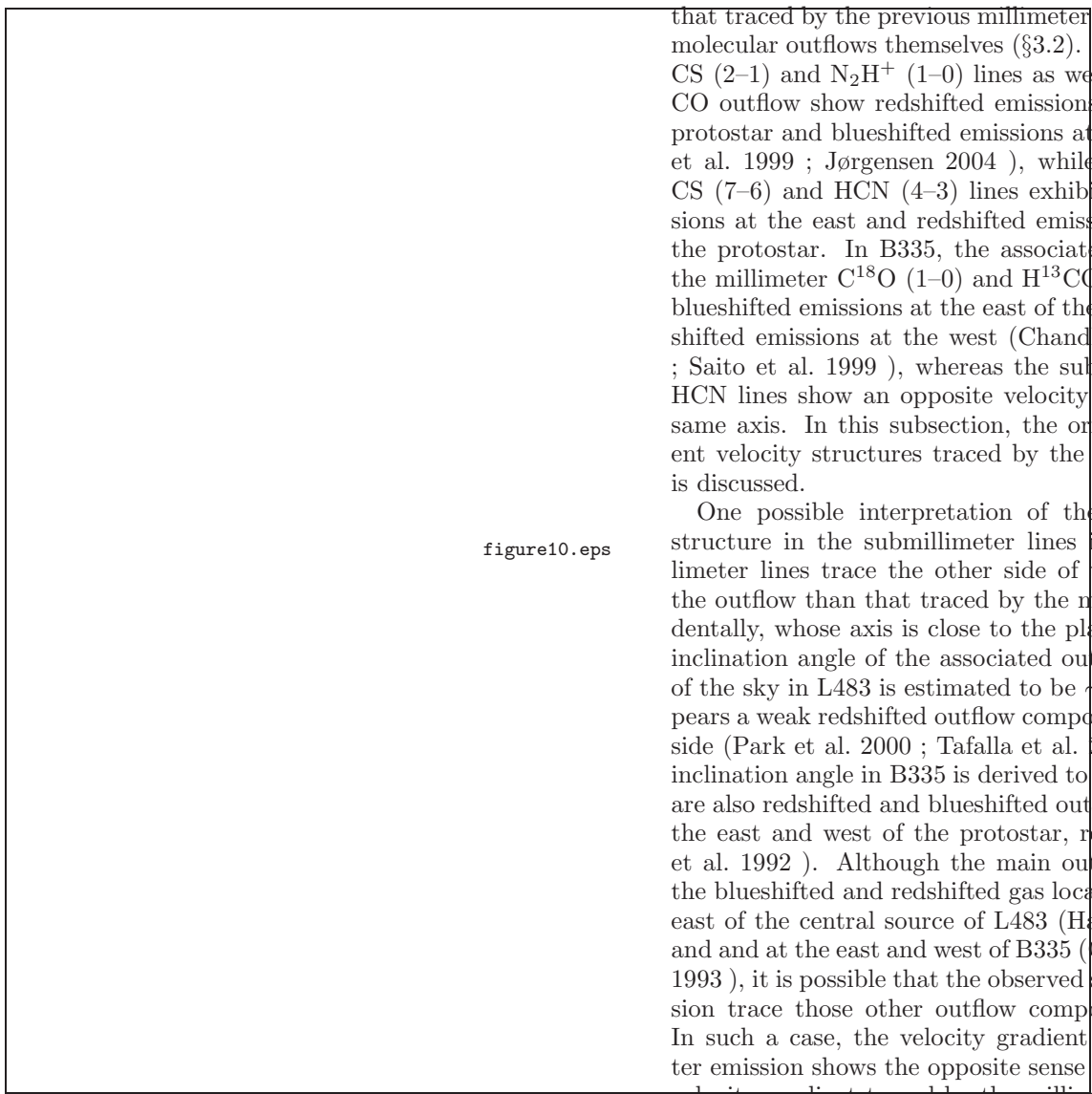


figure10.eps

Fig. 10. Results of our LVG model calculations. Brightness temperatures of the CS (7-6) (left) and HCN (4-3) (right) lines are plotted in contours as a function of the gas density ($\equiv n_{H_2}$) and the molecular abundance per unit velocity gradient ($\equiv X/dv/dr$) at each gas kinetic temperature ($T_k = 10, 20, 40, 60$, and 100 K as shown in the Figure). Contour levels are shown in the Figure, and the lowest five contours correspond to the observed line intensities at the representative positions listed in Table 2.

hydrodynamic model is not adequate to fully explain our observational results. We will discuss on these different velocity structures in the next section.

4.2. Different Velocity Structures traced by the Submillimeter Lines in the Low-mass Protostellar Envelopes

Our submillimeter-line observations of the low-mass protostellar envelopes have revealed that along the axis of the associated molecular outflows the sense of the velocity

gradient traced by the submillimeter lines is opposite to that traced by the previous millimeter observations or the molecular outflows themselves (§3.2). In L483, millimeter CS (2-1) and N_2H^+ (1-0) lines as well as the associated CO outflow show redshifted emissions at the east of the protostar and blueshifted emissions at the west (Hatchell et al. 1999 ; Jørgensen 2004), while the submillimeter CS (7-6) and HCN (4-3) lines exhibit blueshifted emissions at the east and redshifted emissions at the west of the protostar. In B335, the associated CO outflow and the millimeter $C^{18}O$ (1-0) and $H^{13}CO^+$ (1-0) lines show blueshifted emissions at the east of the protostar and redshifted emissions at the west (Chandler & Sargent 1993 ; Saito et al. 1999), whereas the submillimeter CS and HCN lines show an opposite velocity gradient along the same axis. In this subsection, the origin of these different velocity structures traced by the submillimeter lines is discussed.

One possible interpretation of the different velocity structure in the submillimeter lines is that the submillimeter lines trace the other side of the conical shell of the outflow than that traced by the millimeter lines incidentally, whose axis is close to the plane of the sky. The inclination angle of the associated outflow from the plane of the sky in L483 is estimated to be $\sim 45^\circ$ and there appears a weak redshifted outflow component at the western side (Park et al. 2000 ; Tafalla et al. 2000), whereas the inclination angle in B335 is derived to be $\sim 10^\circ$ and there are also redshifted and blueshifted outflow components at the east and west of the protostar, respectively (Hirano et al. 1992). Although the main outflow component of the blueshifted and redshifted gas locates at the west and east of the central source of L483 (Hatchell et al. 1999) and at the east and west of B335 (Chandler & Sargent 1993), it is possible that the observed submillimeter emission trace those other outflow components incidentally. In such a case, the velocity gradient in the submillimeter emission shows the opposite sense to that of the main velocity gradient traced by the millimeter lines. The observed elongation of the submillimeter emission along the outflow axis in L483 favors this interpretation, and the higher-temperature ($\gtrsim 40$ K) gas at the western extension in L483 discussed in the previous subsection may reflect the shock interaction between the outflow and the ambient dense gas (Umemoto et al. 1992 ; Hirano & Taniguchi 2001).

Another possible and more interesting interpretation of the observed velocity structures in the submillimeter lines is an expanding gas motion which is perpendicular to the outflow axis, as shown in Figure 11. This figure demonstrates that the submillimeter lines trace molecular gas at the surface of the flattened disklike envelope, which is being stripped away by some mechanism such as the stellar wind, while the millimeter lines trace infalling gas at the midplane of the envelope. Here, on the side of the blueshifted outflow the expanding gas is observed as a redshifted component and on the side of the redshifted outflow as a blueshifted component, while the infalling gas components show the same velocity gradient as that

of the outflow. Hence, this configuration can explain the different velocity gradient observed in the submillimeter lines from that of the outflow components or infalling gas traced by the millimeter lines.

Similar velocity structures along the perpendicular direction to the polar outflow have also been found in near-infrared observations of young stellar objects. Pyo et al. (2005) have observed lower-velocity [Fe II] winds with a wide opening angle of $\sim 100^\circ$ in L1551 IRS5, as well as well-collimated higher-velocity jets along the polar axis. Comparable results were also obtained for the young T Tauri star DG Tau (Pyo et al. 2003). They suggest that such a wind with a wide opening angle will be effective in sweeping up envelope material from the close vicinity of its driving source. The observed velocity structures in the submillimeter lines may trace such a gas motion in the envelope, although the spatial scale in the submillimeter results (> 2000 AU) is much larger than that of the infrared observations ($\sim 100 - 400$ AU). In L483, the line core emission in the HCO^+ (3–2) line does show the same velocity gradient as our submillimeter results, while the HCO^+ (3–2) line wing emission traces the bipolar outflow itself (see Figure 15 in Gregersen et al. 1997). At the surface of the flattened disklike envelopes molecular gas is irradiated by the stellar photons and hence the gas temperature is likely to be higher than that at the midplane. Then, the warmer surface regions are selectively traced by the submillimeter observations whereas the colder, infalling regions at the midplane are traced by the millimeter lines alone. In fact, Spaans et al. (1995) proposed that the narrow ^{12}CO and ^{13}CO $J=6-5$ emission observed toward many low-mass young stellar objects is produced at the surface of the circumstellar envelope surrounding the cavity evacuated by the bipolar outflow, heated by the radiation field generated in the inner part of the accretion disk. Recent two-dimensional radiative transfer models in protostellar envelopes have also revealed that at the surface of the flattened disklike envelope the gas temperature becomes higher than that predicted from spherically symmetric models (Nakazato et al. 2003; Whitney et al. 2003). The observed submillimeter HCN and CS emission may have such an origin.

The interpretation of the expanding flattened envelope, however, has one weak point, that is, in L483 the observed submillimeter emissions are elongated *along* the outflow direction. If the submillimeter lines trace expanding gas motion at the surface of the disklike envelope, the elongation should be perpendicular to the axis of the associated outflow. In order to compensate for this contradiction, non polar-symmetric geometry and/or the flared shape of the envelope must be incorporated. With the present data, we cannot determine which scenario, the incidental projection effect or the expanding flattened envelope with the flared and/or non polar-symmetric shape, is more plausible.

On the other hand, we have also found an opposite velocity gradient in the submillimeter lines to that in the millimeter lines across the outflow axis in B335. The origin of the difference is less clear, but the expanding gas

figure11.eps

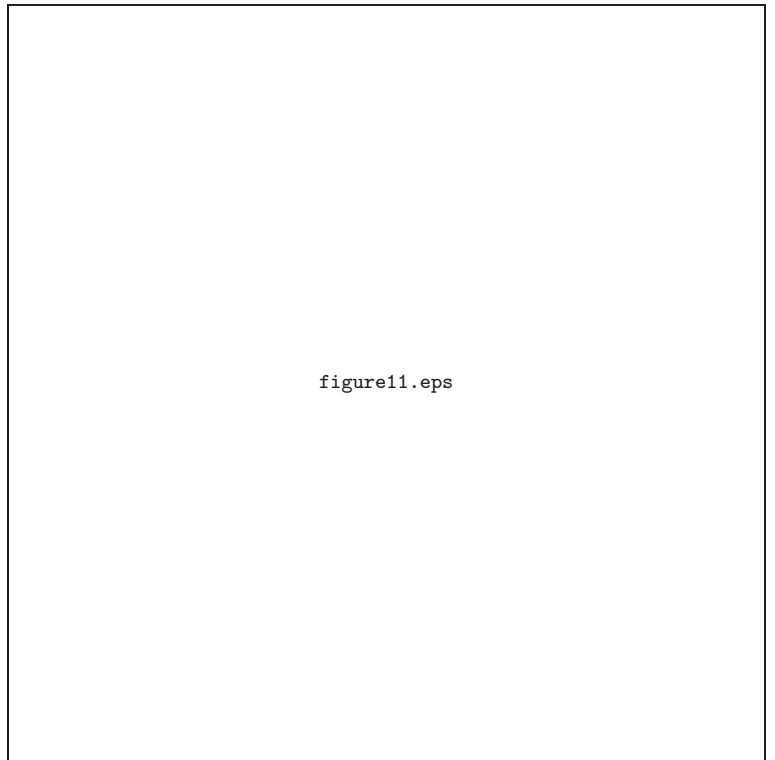


Fig. 11. A schematic diagram to interpret the observed velocity gradient of the submillimeter emission in the low-mass protostellar envelopes. Observers' line of sight is normal to the paper. The bold black ellipse represents a flattened disklike envelope. This disklike envelope is tilted, and the near side is to the left. The associated blueshifted and redshifted molecular outflows perpendicular to the disklike envelope are shown in light blue and red colors, respectively, and the blueshifted outflow locates at the lefthand, near side. At the midplane of the disklike envelope there is an infalling gas motion as described in the black arrows. At the surface of the disklike envelope there is an expanding gas motion as shown in red and blue arrows, which is traced by the present submillimeter observations. Here, the left-half portion is redshifted while the other half blueshifted, and this velocity structure has an opposite sense to that of the outflow or the infalling gas motion. The configuration in this diagram represents the case of B335. For the case of L483 one can just flip this configuration horizontally.

traced by the submillimeter lines may have a different rotational motion. In any sense, our new submillimeter mapping observations have presented us an implication that submillimeter lines trace different kinematics from that traced by millimeter lines, and that there is another velocity structure which previous millimeter observations could not find in low-mass protostellar envelopes.

5. Summary

We have made mapping observations of low-mass protostellar envelopes of L483 and B335 as well as a single-point observation of L723 in the HCN ($J=4-3$) and CS ($J=7-6$) lines with ASTE. Main results of our new submillimeter

observations are summarized as follows.

- 1 We have detected both the HCN and CS lines toward all the sources. Typical intensities and line widths are 0.5 K and 2.0 km s⁻¹ in the HCN line and 1.0 K and 1.5 km s⁻¹ in the CS line, respectively. The CS-to-HCN intensity ratio is similar across the three samples (2.1 - 2.5), and there may be a correlation between the source luminosity and the intensity of the submillimeter lines.
- 2 Mapping observations of L483 in the HCN and CS lines show that the submillimeter emissions are extended to the west of the protostar, consistent with the distribution of the dust continuum emission, and that the deconvolved size is ~ 5500 AU \times 3700 AU (P.A. = 78°) in the HCN emission. The extent of the submillimeter emissions in L483 implies the presence of higher-temperature ($\gtrsim 40$ K) or higher-density ($\gtrsim 6 \times 10^6$ cm⁻³) gas at 4000 AU away from the central protostar. The existence of such high-temperature or high-density gas at 4000 AU away from the protostar is unlikely to be explained via heating from the central protostar with the spherically symmetric geometry in the envelope.
- 3 Both in L483 and B335, we found velocity gradients in the submillimeter lines along and across the axis of the associated molecular outflow. The sense of the velocity gradient traced by the submillimeter lines along the outflow direction is opposite to that of the results from the previous millimeter observations or the associated molecular outflow itself, both in L483 and B335. One possible interpretation of the different velocity gradient is that the submillimeter lines trace the other side of the conical shape of the outflow incidentally, where the outflow axis is close to the plane of the sky. Alternatively, expanding gas motions at the surface of the flattened disklike envelopes, or gas motions to strip off the envelope, irradiated from the central star directly, can explain the observed submillimeter velocity structure.

We are grateful to R. Kawabe and N. Ohashi for their fruitful discussions. We thank all the ASTE staff for their dedicated support of the telescope and observatory operations. We acknowledge the anonymous referee, whose comments polish up the manuscript significantly.

References

Anglada, G., Estalella, R., Rodríguez, L. F., Torrelles, J. M., López, R., & Cantó, J. 1991, *ApJ*, 376, 615

Barsony, M. 1995, in *ASP Conf. Ser.* 65, *Cloud, Cores and Low Mass Stars*, ed D. P. Clemens & R. Barvainis, (San Francisco: ASP), 197

Blake, G. A., van Dishoeck, E. F., Jansen, D. J., Groesbeck, T. D., & Mundy, L. G. 1994, *ApJ*, 428, 680

Buckle, J. V., Hatchell, J., & Fuller, G. A. 1999, *A&A*, 348, 584

Ceccarelli, C., Castets, A., Caux, E., Hollenbach, D., Loinard, L., Molinari, S., & Tielens, A. G. G. M. 2000, *A&A*, 355, 1129

Chandler, C. J., & Sargent, A. I. 1993, *ApJL*, 414, L29

Choi, M., Evans II, N. J., Gregeren, E. M., & Wang, Y. 1995, *ApJ*, 448, 742

Davidson, J. A. 1987, *ApJ*, 315, 602

Evans II, N. J., Lee, J.-E., Rawlings, J. M. C., & Choi, M. 2005, *ApJ*, 626, 919

Ezawa, H., Kawabe, R., Kohno, K., & Yamamoto, S. 2004, *Proc. SPIE*, 5489, 763

Fuller, G. A., & Wootten, A. 2000, *ApJ*, 534, 854

Goldreich, P., & Kwan, J. 1974, *ApJ*, 189, 441

Green, S., & Chapman, S. 1978, *ApJS*, 37, 169

Green, S., & Thaddeus, P. 1974, *ApJ*, 191, 653

Gregeren, E. M., Evans II, N. J., Zhou, S., & Choi, M. 1997, *ApJ*, 484, 256

Harvey, D. W. A., Wilner, D. J., Myers, P. C., Tafalla, M., & Mardones, D. 2003a, *ApJ*, 583, 809

Harvey, D. W. A., Wilner, D. J., Myers, P. C., & Tafalla, M. 2003b, *ApJ*, 596, 383

Hatchell, J., Fuller, G. A., & Ladd, E. F. 1999, *A&A*, 344, 687

Hayashi, S. S., Hasegawa, T., & Kaifu, N. 1991, *ApJ*, 377, 492

Hirano, N., Kameya, O., Kasuga, T., & Umemoto, T. 1992, *ApJL*, 390, L85

Hirano, N., Hayashi, S. S., Umemoto, T., & Ukita, N. 1998, *ApJ*, 504, 334

Hirano, N., & Taniguchi, Y. 2001, *ApJL*, 550, L219

Hogerheijde, M. R., van Dishoeck, E. F., Blake, G. A., & van Langevelde, H. J. 1998, *ApJ*, 502, 315

Hogerheijde, M. R., van Dishoeck, E. F., Salverda, J. M., & Blake, G. A. 1999, *ApJ*, 513, 350

Jewitt, D. C., Matthews, H. E., Owen, T., & Meier, R. 1997, *Science*, 278, 90

Jørgensen, J. K., Schöier, F. L., & van Dishoeck, E. F. 2002, *A&A*, 389, 908

Jørgensen, J. K., Schöier, F. L., & van Dishoeck, E. F. 2004, *A&A*, 416, 603

Jørgensen, J. K. 2004, *A&A*, 424, 589

Kohno, K. 2005, in *ASP Conf. Ser.* 344, *The Cool Universe: Observing Cosmic Dawn*, ed C. Lidman & D. Alloin, (San Francisco: ASP), 242

Ladd, E. F., Adams, F. C., Casey, S., Davidson, J. A., Fuller, G. A., Harper, D. A., Myers, P. C., & Padman, R. 1991, *ApJ*, 366, 203

Lay, O. P., Carlstrom, J. E., Hills, R. E., & Phillips, T. G. 1994, *ApJL*, 434, L75

Mardones, D., Myers, P. C., Tafalla, M., Wilner, D. J., Bachiller, R., & Garay, G. 1997, *ApJ*, 489, 719

Masunaga, H., Miyama, S. M., & Inutsuka, S. 1998, *ApJ*, 495, 346

Masunaga, H., & Inutsuka, S. 2000, *ApJ*, 531, 350

Moriarty-Schieven, G. H., Wannier, P. G., Mangum, J. G., Tamura, M., & Olmsted, V. K. 1995, *ApJ*, 455, 190

Myers, P. C., Bachiller, R., Caselli, P., Fuller, G. A., Mardones, D., Tafalla, M., & Wilner, D. J. 1995, *ApJL*, 449, L65

Nakazato, T., Nakamoto, T., & Umemura, M. 2003, *ApJ*, 583, 322

Ohashi, N., Hayashi, M., Ho, P. T. P., Momose, M., & Hirano, N. 1996, *ApJ*, 466, 957

Ohashi, N., Hayashi, M., Ho, P. T. P., & Momose, M. 1997a, *ApJ*, 475, 211

Ohashi, N., Hayashi, M., Ho, P. T. P., Momose, M., Tamura, M., Hirano, N., & Sargent, A. I. 1997b, *ApJ*, 488, 317

Osorio, M., D'Alessio, P., Muzerolle, J., Calvet, N., & Hartmann, L. 2003, *ApJ*, 586, 1148

Park, Y.-S., Panis, J.-F., Ohashi, N., Choi, M., & Minh, Y. C. 2000, *ApJ*, 542, 344

Pyo, T.-S., Hayashi, M., Kobayashi, N., Terada, H., Goto, M., Yamashita, T., Tokunaga, A. T., & Itoh, Y. 2003, *ApJ*, 590, 340

Pyo, T.-S., Hayashi, M., Kobayashi, N., Tokunaga, A. T., Terada, H., Tsujimoto, M., Hayashi, S. S., Usuda, T., Yamashita, T., Takami, H., Takato, N., & Nedachi, K. 2005, *ApJ*, 618, 817

Saito, M., Sunada, K., Kawabe, R., Kitamura, Y., & Hirano, N. 1999, *ApJ*, 518, 334

Saito, M., Kawabe, R., Kitamura, Y., & Sunada, K. 2001, *ApJ*, 547, 840

Scoville, N. Z., & Solomon, P. M. 1974, *ApJL*, 187, L67

Spaans, M., Hogerheijde, M. R., Mundy, L. G., & Van Dishoeck, E. F. 1995, *ApJL*, 455, L167

Tafalla, M., Myers, P. C., Mardones, D., & Bachiller, R. 2000, *A&A*, 359, 967

Takakuwa, S., Mikami, H., Saito, M., & Hirano, N. 2000, *ApJ*, 542, 367

Takakuwa, S., Ohashi, N., & Hirano, N. 2003, *ApJ*, 590, 932

Takakuwa, S., Ohashi, N., Ho, P. T. P., Chunhua, Q., Wilner, D. J., Qizhou, Z., Bourke, T. L., Hirano, N., Choi, M., & Yang, J. 2004, *ApJL*, 616, L15

Takakuwa, S., et al. 2006, *ApJ*, submitted

Umemoto, T., Iwata, T., Fukui, Y., Mikami, H., Yamamoto, S., Kameya, O., & Hirano, N. 1992, *ApJL*, 392, L83

van Dishoeck, E. F., Blake, G. A., Jansen, D. J., & Groesbeck, T. D. 1995, *ApJ*, 447, 760

Whitney, B. A., Wood, K., Bjorkman, J. E., & Wolff, M. J. 2003, *ApJ*, 591, 1049

Wilner, D. J., Myers, P. C., Mardones, D., & Tafalla, M. 2000, *ApJL*, 544, L69

Winnewisser, G., Churchwell, E., & Walmsley, C. M. 1979, in *Modern Aspects of Microwave Spectroscopy*, ed. G. W. Chantry (New York: Academic), p.313.

Zhou, S. 1995, *ApJ*, 442, 685

This figure "figure1.gif" is available in "gif" format from:

<http://arxiv.org/ps/astro-ph/0608100v1>

This figure "figure2.gif" is available in "gif" format from:

<http://arxiv.org/ps/astro-ph/0608100v1>

This figure "figure3.gif" is available in "gif" format from:

<http://arxiv.org/ps/astro-ph/0608100v1>

This figure "figure4.gif" is available in "gif" format from:

<http://arxiv.org/ps/astro-ph/0608100v1>

This figure "figure5.gif" is available in "gif" format from:

<http://arxiv.org/ps/astro-ph/0608100v1>

This figure "figure6.gif" is available in "gif" format from:

<http://arxiv.org/ps/astro-ph/0608100v1>

This figure "figure7.gif" is available in "gif" format from:

<http://arxiv.org/ps/astro-ph/0608100v1>

This figure "figure8.gif" is available in "gif" format from:

<http://arxiv.org/ps/astro-ph/0608100v1>

This figure "figure9.gif" is available in "gif" format from:

<http://arxiv.org/ps/astro-ph/0608100v1>

This figure "figure10.gif" is available in "gif" format from:

<http://arxiv.org/ps/astro-ph/0608100v1>

This figure "figure11.gif" is available in "gif" format from:

<http://arxiv.org/ps/astro-ph/0608100v1>